論文 / 著書情報
Article / Book Information

Title	Calculation of isotropic turbulence using a pure Lagrangian vortex method
Authors	Rio Yokota, Tarun Kumar Sheel, Shinnosuke Obi
Citation	Journal of Computational Physics, Vol. 226, , pp. 1589–1606
Pub. date	2007, 6
DOI	http://dx.doi.org/10.1016/j.jcp.2007.06.003
Note	このファイルは著者（最終）版です。 This file is author (final) version.
Creative Commons	See next page.

License

Calculation of Isotropic Turbulence Using a Pure Lagrangian Vortex Method

R. Yokota *, T. K. Sheel and S. Obi

Department of Mechanical Engineering, Keio University, 3-14-1 Hiyoshi, Kohoku-Ku, Yokohama 223-8522, Japan

Abstract

The vortex method is applied to the calculation of a decaying homogeneous isotropic turbulence of $Re_\lambda = 25, 50$ and the results are compared with a spectral method calculation. Vortex method calculations were accelerated by the use of a fast multipole method for periodic boundary conditions. The core spreading method and particle strength exchange were selected as the viscous diffusion scheme. The effect of spatial resolution was examined along with Reynolds number dependence and the effect of spatial adaption of elements.

Key words: Vortex methods; Isotropic turbulence; Core spreading method; Particle strength exchange; Fast multipole methods

* Corresponding author. Fax: +81 45 566 1495
Email address: rioyokota@a5.keio.jp (R. Yokota).

1 Introduction

The simulation of turbulence requires the accurate prediction of the production, transport, and dissipation of kinetic energy. In vortex methods, this is made possible by properly calculating the stretching term and diffusion term of the vorticity equation. Although vortex methods have made remarkable advancements in the past decade, they still face numerous challenges, especially involving viscous diffusion schemes. The mesh-free nature of the pure Lagrangian vortex methods itself is a large advantage, but it is also the primary source of this viscous diffusion problem. To solve these problems, numerous viscous diffusion schemes have been proposed during the past quarter century, along with spatial adaption schemes to handle the distortion of particles. It is important to first validate these schemes in an environment, isolated from mean shear and near wall effects, but still complex enough to represent general turbulent behavior, i.e. the cascade and decay of kinetic energy. The homogeneous isotropic turbulence is an ideal test case in this sense, and has been used to validate grid based direct numerical simulations (DNS) in the past. We believe the same can be done for vortex methods, as the first step toward developing a mesh-free but rigorous turbulence simulation.

Only a small number of vortex methods have been tested for the homogeneous isotropic turbulence, despite its significance. Cottet et al. [1] used the vortex-in-cell for the viscous diffusion scheme and compared with a spectral method for $N = 128^3$ grid points. The evolution of the energy spectrum, kinetic energy, dissipation, enstrophy and skewness were in excellent agreement. However, their method requires the use of a grid for the stretching and velocity calculations, leaving only the convection to be calculated using a La-

grangian discretization. Totsuka & Obi [2] compared the spectral method with the vortex method using the core spreading method and a Laplacian model used in the moving particle semi-implicit (MPS) [3], which is similar to the redistribution method in vortex methods. All calculations are preformed in 2-D and no spatial refinement is used in the core spreading method. They use a particle insertion and merging technique for the MPS Laplacian method and the energy spectrum agrees with the spectral method for this case. Since the stretching term does not exist in the 2-D vorticity equation, their calculation can be thought of as an assessment of the diffusion term only. It is necessary to extend this to a 3-D flow and evaluate the balance between stretching and dissipation, in order to validate both the cascade and dissipation of kinetic energy in pure Lagrangian vortex methods.

The absence of vortex method applications to homogeneous isotropic turbulence can be explained by its comparative inefficiency for this particular flow. The calculation cost becomes high compared to spectral methods because vortex methods do not benefit from periodic boundary conditions, whereas the spectral methods enormously do. Even with the use of fast algorithms, the speed of a N-body calculation is several orders lower than a grid based fast Poisson solver as noted by Cottet et al. [1]. Though, the vortex method would become advantageous for external flows, where the vorticity is confined to a finite region near the wall.

In the present study, an acceleration technique for the Biot-Savart calculation in a periodic domain is developed and validated. With the help of this acceleration technique, the 3-D isotropic turbulence is calculated using a pure Lagrangian vortex method. A spectral method calculation using the same number of elements N, Reynolds number Re_λ and initial condition, is used as

reference. The particle strength exchange (PSE) and core spreading method (CSM) are selected as viscous diffusion schemes for the vortex method to consider both possibilities. This study first concentrates on the time evolution of the kinetic energy spectrum, where the reproducibility of the energy cascade is examined. Our focus then moves on to the decay of kinetic energy and enstrophy. The velocity derivative skewness and flatness are also examined to ascertain the soundness of higher order statistics. Subsequently, the dependence on spatial resolution and Reynolds number is studied, in order to generalize our observations. Following that, we observe the spectral energy transfer from a different perspective by plotting all terms of the energy spectrum equation. Finally, the effect of spatial adaption is investigated for both viscous diffusion schemes.

2 Numerical Method

2.1 Viscous Diffusion

The extension of vortex methods to viscous flows has not been a straightforward task, and the diversity of methods has become quite large. The random vortex method (RVM) by Chorin [4] uses a stochastic interpretation of the diffusion equation. It has served an important role in the early development of viscous diffusion schemes, but its slow convergence rate prompted the development of alternative methods. The core spreading method (CSM) by Kuwahara & Takami [5] or Leonard [6] uses a deterministic approach, which changes the standard deviation of the Gaussian distribution of vorticity to match the fundamental solution of the diffusion equation. A straightforward implementation

of this method lacks convergence due to the fact that the ever-expanding Gaussian distribution moves with the velocity at its center. Local spatial refinement [7] can circumvent this problem, though this will introduce a large amount of error without careful consideration [8][9].

The particle strength exchange (PSE) by Degond & Mas-Gallic [10] redistributes the strength among vortex elements by solving the integral equation of the Laplacian operator. The location of elements are used as quadrature points, thus requires them to be nearly uniform for an accurate calculation. In highly strained fields this is impossible without frequent regridding, which will sacrifice the grid-free nature and also accumulate numerical diffusion error without careful selection of the interpolation scheme [11]. The vortex redistribution method (VRM) by Shankar & van Dommelen [12] also redistributes the strength of vortex elements but by solving an underdetermined system of equations to equate the truncated Taylor series of the new distribution with that of the exactly diffused vorticity. Although, restrictions of particle nonuniformity are not as severe as the PSE, it is obvious that a sufficient number must exist in the neighborhood. The insertion and merging of particles is still an open area of research, as is the case with splitting and merging particles in CSMs.

In most cases a vortex element has three properties, vortex strength, core radius, and velocity. The CSM changes the core radius, PSE and VRM change the vortex strength to account for diffusion. The diffusion velocity method by Ogami & Akamatsu [13] modifies the velocity instead, where the diffusion velocity becomes the product of $-\nu/\omega$ and the gradient of vorticity. For regions of zero vorticity the $-\nu/\omega$ becomes singular, so an algorithm which does not increase the vorticity magnitude outside of the computational vorticity sup-

port [14] is essential to this scheme. There exist many other ways to calculate the viscous diffusion of vorticity using a semi-Lagrangian discretization, such as the vortex in cell (VIC), free Lagrangian, triangulated, and moving least squares (MLS). The present study focuses on pure Lagrangian schemes (with remeshing in some cases), thus semi-Lagrangian methods are out of scope.

In particular, we will focus on two of these viscous diffusion schemes -the PSE and CSM-. The PSE is favorable in the sense that, it permits the use of higher order kernels, does not require viscous splitting, and is a straightforward solution to the governing integral equation. It has also been successfully implemented in many applications. On the other hand, the CSM has the potential of becoming a pure Lagrangian scheme, despite its reputation it once suffered from. Unlike, other viscous diffusion methods the CSM does not require the use of any kind of mesh whatsoever, even for spatial adaption. Furthermore, the spatial adaption can be performed in a less ambiguous manner compared to the VRM.

The PSE and CSM contrast with each other in many aspects, starting from the physical property it changes, to the way it handles spatial adaptation of elements. It is worth investigating how these differences affect the performance of the vortex method for the homogeneous isotropic turbulence. The details of the vortex blob method for the two schemes are discussed below.

Both the CSM and PSE are ways to discretize the viscous diffusion equation

$$\frac{D\boldsymbol{\omega}_i}{Dt} = \nu \nabla^2 \boldsymbol{\omega}_i, \tag{1}$$

where the Green's function solution is

$$\boldsymbol{\omega}_i = \frac{\boldsymbol{\gamma}_j}{(4\pi\nu t)^{d/2}} \exp\left(-\frac{\mathbf{r}_{ij}^2}{4\nu t}\right). \tag{2}$$

$\boldsymbol{\omega}$ is the vorticity, ν is the kinematic viscosity, $\boldsymbol{\gamma}$ is the vortex strength, $\mathbf{r}_{ij} = |\mathbf{x}_i - \mathbf{x}_j|$ is the distance vector, $\mathbf{x}$ is the position vector, and d is the dimensionality of the problem. The subscript i stands for the target elements, while j stands for the source elements. The vortex blob method uses a smoothing function ζ_σ to discretize the diffusion equation. In this case the vorticity at an arbitrary point can be expressed as

$$\boldsymbol{\omega}_i = \sum_j \boldsymbol{\gamma}_j \zeta_\sigma\left(\mathbf{r}_{ij}\right). \tag{3}$$

A common choice for the smoothing function is the Gaussian distribution

$$\zeta_\sigma = \frac{1}{(2\pi\sigma^2)^{d/2}} \exp\left(-\frac{\mathbf{r}_{ij}^2}{2\sigma^2}\right). \tag{4}$$

By substituting (4) into (3), it can be seen that changing the variance of the Gaussian distribution according to

$$\sigma^2 = 2\nu t \tag{5}$$

will result in the heat kernel (2). σ is often referred to as the core radius of the vortex blob, and represents the physical length scale of the vortex elements. The PSE solves an integral equation for the Laplacian operator

$$\nabla^2\boldsymbol{\omega}_i = \frac{2}{\sigma^2}\sum_j \eta_\sigma\left(\mathbf{r}_{ij}\right)\left(\boldsymbol{\omega}_j - \boldsymbol{\omega}_i\right) \tag{6}$$

where the PSE kernel is

$$\eta_\sigma = \frac{1}{(2\pi\sigma^2)^{d/2}} \exp\left(-\frac{\mathbf{r}_{ij}^2}{2\sigma^2}\right). \tag{7}$$

The Gaussian smoothing function (4) and Gaussian PSE kernel (7) are identical. So by assuming $\sigma^2 = 2\nu t$ the PSE kernel will also reduce to the heat

kernel. However, unlike the CSM we do not change σ, but substitute (6) and (7) into (1) to obtain the rate of change of the vortex strength

$$\frac{D\boldsymbol{\gamma}_i}{Dt} = \sum_j \left(V_j\boldsymbol{\gamma}_j - V_i\boldsymbol{\gamma}_i\right)\frac{2\nu}{\sigma^2}\frac{1}{\left(2\pi\sigma^2\right)^{d/2}}\exp\left(-\frac{\mathbf{r}_{ij}^2}{2\sigma^2}\right), \tag{8}$$

where V is the volume of the vortex element.

In a numerical sense, calculating the exponential function for a N-body calculation is time consuming, and the Gaussian function is not the only choice for the smoothing function. They only need to satisfy certain moment properties [15]. The high order algebraic function by Winckelmans [16] is second order, and has a simple algebraic form. We will use this for the smoothing function and PSE kernel, which have the form

$$\zeta_\sigma = \frac{15}{8\pi}\frac{\sigma^4}{(\mathbf{r}_{ij}^2+\sigma^2)^{7/2}}, \tag{9}$$

$$\eta_\sigma = \frac{105}{8\pi}\frac{\sigma^6}{(\mathbf{r}_{ij}^2+\sigma^2)^{9/2}}. \tag{10}$$

2.2 Fast Multipole Method

The Biot-Savart equation

$$\mathbf{u}_i = \sum_{j=1}^{N}\boldsymbol{\gamma}_j g_\sigma \times \nabla G, \tag{11}$$

and the stretching term

$$\begin{aligned}\frac{D\boldsymbol{\gamma}_i}{Dt} &= \boldsymbol{\gamma}_i\cdot\nabla\mathbf{u}_i \\ &= \boldsymbol{\gamma}_i\cdot\nabla\sum_{j=1}^{N}\boldsymbol{\gamma}_j g_\sigma\times\nabla G \\ &= \sum_{j=1}^{N}\boldsymbol{\gamma}_j g_\sigma\times\nabla\nabla G\cdot\boldsymbol{\gamma}_i,\end{aligned} \tag{12}$$

are calculated using the fast multipole method(FMM) in order to reduce the complexity from $O(N^2)$ to $O(N)$. G is the Green's function of the Laplace equation. g_σ is the cutoff function, which is defined by $g_\sigma = \int_0^\rho \zeta s^{d-1} ds$, where $\zeta\left(\frac{|\mathbf{x}|}{\sigma}\right) = 2^{d-1}\pi\sigma^d\zeta_\sigma(\mathbf{x})$, and d is the dimension. For our case

$$G = \frac{1}{4\pi r_{ij}}, \tag{13}$$

$$g_\sigma = \frac{r_{ij}^2 + 5/2\sigma^2}{(r_{ij}^2 + \sigma^2)^{5/2}} r_{ij}^3. \tag{14}$$

For the FMM equations, we will adopt the conventions used by Cheng et al. [17]. By doing so, the Green's function can be approximated by the multipole expansion

$$\sum_{j=1}^{N} G \approx \frac{1}{4\pi} \sum_{n=0}^{p} \sum_{m=-n}^{n} \underbrace{r_i^{-n-1} Y_n^m(\theta_i, \phi_i)}_{S_i} \left\{ \sum_{j=1}^{N} \underbrace{\rho_j^n Y_n^{-m}(\alpha_j, \beta_j)}_{M_j} \right\}, \tag{15}$$

and also the local expansion

$$\sum_{j=1}^{N} G \approx \frac{1}{4\pi} \sum_{n=0}^{p} \sum_{m=-n}^{n} \underbrace{r_i^{n} Y_n^m(\theta_i, \phi_i)}_{R_i} \left\{ \sum_{j=1}^{N} \underbrace{\rho_j^{-n-1} Y_n^{-m}(\alpha_j, \beta_j)}_{L_j} \right\}. \tag{16}$$

We define the operators S, M, R, L to simplify the equations in the following steps. Using these operators, (11) can be written as

$$\mathbf{u}_i \approx \frac{1}{4\pi} \sum_{n=0}^{p} \sum_{m=-n}^{n} \left\{ \sum_{j=1}^{N} \boldsymbol{\gamma}_j M_j \right\} \times \nabla S_i, \tag{17}$$

$$\mathbf{u}_i \approx \frac{1}{4\pi} \sum_{n=0}^{p} \sum_{m=-n}^{n} \left\{ \sum_{j=1}^{N} \boldsymbol{\gamma}_j L_j \right\} \times \nabla R_i. \tag{18}$$

Similarly, (12) can be written as

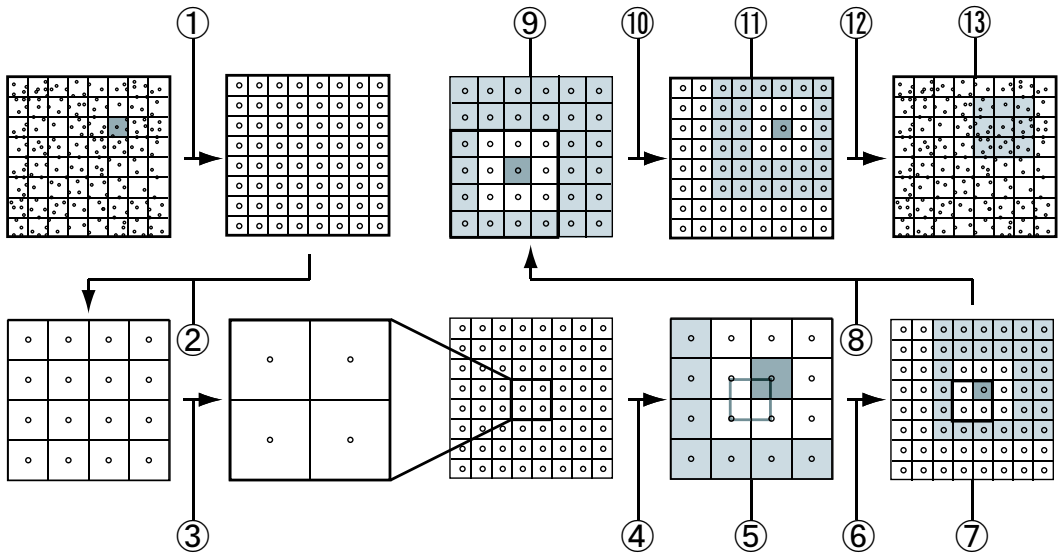

Fig. 1. Flow of periodic FMM calculation

$$\frac{D\boldsymbol{\gamma}_i}{Dt} \approx \frac{1}{4\pi} \sum_{n=0}^{p} \sum_{m=-n}^{n} \left\{ \sum_{j=1}^{N} \boldsymbol{\gamma}_j \nabla M_j \right\} \times (\boldsymbol{\gamma}_i \cdot \nabla S_i)\,, \tag{19}$$

$$\frac{D\boldsymbol{\gamma}_i}{Dt} \approx \frac{1}{4\pi} \sum_{n=0}^{p} \sum_{m=-n}^{n} \left\{ \sum_{j=1}^{N} \boldsymbol{\gamma}_j \nabla L_j \right\} \times (\boldsymbol{\gamma}_i \cdot \nabla R_i)\,. \tag{20}$$

The cutoff function does not appear in these equations since they are used to calculate the effect of the far field, for which it would have negligible effect.

The entire calculation process requires an efficient method for indexing and bookkeeping of the particles and boxes in each level. For the indexing and bookkeeping we adopt the method by Gumerov & Duraiswami [18].

The calculation of homogeneous isotropic turbulence assumes periodicity in all directions. In the present study the FMM is modified to include the effect of periodic images. The flow of calculation is basically the same as the FMM, except for the few steps being added to account for the periodic images. A schematic of the flow of calculation is shown in Fig. 1. The heavy black line represents the original domain without periodic images.

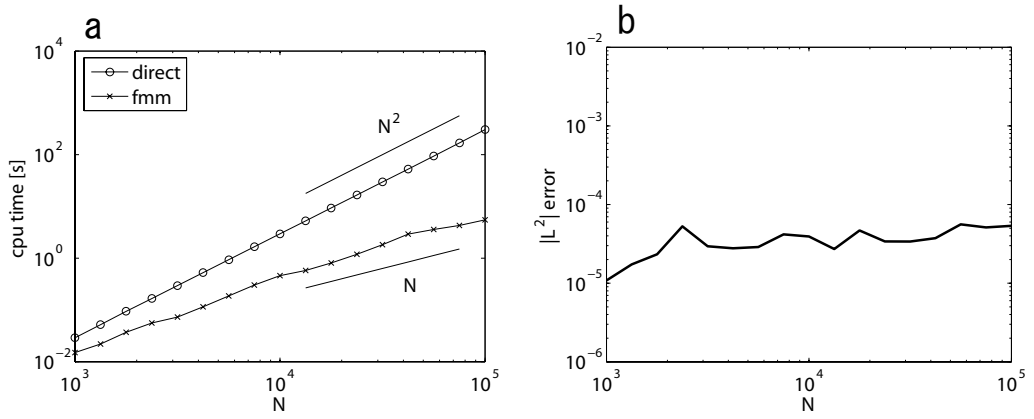

Fig. 2. (a) Cputime of Biot-Savart calculation. (b) L^2 norm error of Biot-Savart calculation.

Steps 1 and 2 are identical to that of the original FMM. The usual FMM does not calculate step 3 because there will be no non-neighboring boxes to calculate the multipole to local translation. Step 4 groups the boxes outside the original domain. Step 5 represents the multipole to local translation at the coarsest level. Step 6 is the local to local translation, and step 7 is the multipole to local translation for the remaining boxes. Step 8 is the local to local translation, which brings us down to the coarsest level in a usual FMM. Steps 9 and 11 are different from the multipole to local translation of a standard FMM, in the sense that it requires the calculation of remaining boxes outside of the original domain. Steps 10, 12 and 13 are identical to the corresponding sequences in a standard FMM.

The most time consuming parts of the FMM are the multipole to local translation in step 11, and the direct calculation in 13 , and this does not change for the periodic FMM. In other words, the additional cost of considering the periodic images is negligible compared to these steps. In a similar manner to the original FMM, steps 2, 10, and 11 are calculated more than once for calculations using more box divisions. Additionally, steps 4, 6, and 7 can be

calculated more than once to consider more periodic image boxes. Step 5 in Fig. 1 considers $N_{box} = 1.5$ periodic image boxes in one direction. By calculating Step 5 for a box twice as large, we can consider the effect of $N_{box} = 3.5$ images and so on.

The Biot-Savart calculation is performed to evaluate the cpu-time for different element numbers. The cpu-time of the Biot-Savart calculation for one time step is plotted against the number of elements in Fig. 2. The L^2 norm error between the direct calculation and FMM calculations are also shown. The number of elements is changed from $10^3 - 10^5$. With the use of the FMM the complexity is reduced from $O(N^2)$ to $O(N)$, while the L^2 norm remains below 10^-4.

2.3 Spectral Method

The spectral Galerkin method with primitive variable formulation is used in the present study. When the pressure term is eliminated by considering the pressure Poisson equation in wave space, we have

$$\hat{\mathbf{u}}_{\mathbf{k}}^{n+1} = \hat{\mathbf{u}}_{\mathbf{k}}^{n} - \Delta t \nu k^2 \hat{\mathbf{u}}_{\mathbf{k}}^{n} - \Delta t \widehat{(\mathbf{u}^n \cdot \nabla \mathbf{u}^n)}_{\mathbf{k}} + \Delta t \frac{\mathbf{k}}{k^2} \left[\mathbf{k} \cdot \widehat{(\mathbf{u}^n \cdot \nabla \mathbf{u}^n)}_{\mathbf{k}} \right]. \qquad (21)$$

This is the actual equation which we solve, where $\hat{\mathbf{u}}_{\mathbf{k}}$ is the velocity in wave number space, $\mathbf{k}$ is the wave number vector. A pseudo-spectral method was used to compute the convolution sums, and the aliasing error was removed by the 3/2-rule. The time integration was performed using the fourth order Runge-Kutta method for all terms. No forcing was applied to the calculation, since it would be difficult to do so in vortex methods.

3 Homogeneous Isotropic Turbulence

The objective of this calculation is to verify the accuracy of the stretching and diffusion in vortex blob methods by directly comparing them with a spectral method. We do not intend to make any new findings about the flow field itself, but rather validate the performance of vortex methods by making use of the unique properties of this flow. The homogeneous isotropic turbulence does not involve global shear, strain, rotation, nor near wall effects, but it does involve a typical energy cascade from large to small scales. Therefore, we can isolate the viscous diffusion error from Lagrangian distortion and near wall effects, and at the same time validate the balance between the stretching and diffusion. Just because the convergence of the Euler equation and diffusion equation have separately been proved, does not mean we can take for granted that the energy cascade will be calculated correctly, because there will always be numerical errors. We would like to shed some light on how many blobs are actually necessary to resolve a calculation of a certain Reynolds number using vortex methods.

3.1 Initial Condition

The initial condition was generated in Fourier space as a solenoidal isotropic velocity field with random phases and a prescribed energy spectrum

$$E \sim k^4 \exp\left(-\frac{2k^2}{k_p^2}\right), \tag{22}$$

and Fourier transformed to physical space [21]. $k_p = 4$ is the peak wave number. The grid points are equally spaced and the calculation domain is $[0, 2\pi]^3$. The resulting initial velocity field has a Gaussian distribution and zero mean.

The spectral method calculation uses this initial condition directly.

The initial condition of the vortex method is generated as follows. First, the vortex elements are placed at the center of a box having grid points at all corners. The vorticity at the center is calculated from the velocity at the corners using a forth order central difference method. The strength of the vortex elements were calculated from this vorticity by solving a system of equations for (3) by using a method described in section 3.7. The core radius of the vortex elements are set to $2\pi/N$ and the overlap ratio is 1.

The vortex method calculation is performed without the use of a grid. The velocity and stretching term calculation are performed by the periodic FMM. The diffusion is calculated by either updating the cutoff radius or vortex strength for the CSM and PSE, respectively. The PSE calculation is embedded in the direct calculation part of the periodic FMM stretching routine. The position, vortex strength and cutoff radius are updated by a second order Adams-Bashforth method. Vortex elements are convected according to the periodic boundary condition, so if an element moves out from one side it comes in from the opposite side. For the energy spectrum calculation of the vortex method, the velocity on the grid is calculated using the Biot-Savart law, and then transformed to wave number space.

The accuracy of this initialization procedure is confirmed by comparing the energy spectrum before and after the initialization. If this error turns out to be negligible compared to the error in the vortex method itself, we can say that our measures for initialization and energy spectrum calculation are adequate for the present investigation.

In Fig. 3 the kinetic energy spectrum before and after the initialization pro-

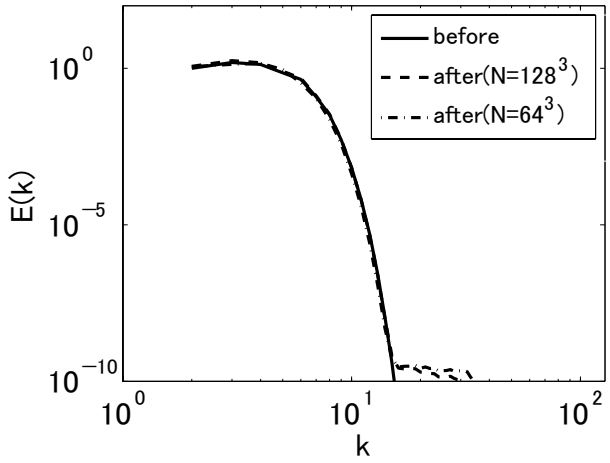

Fig. 3. Energy Spectrum Before and After Initialization

cedure are shown for different spatial resolution. The total error involved in steps 2 and 4 are small enough to produce a strict correspondence with the prescribed energy spectrum for a range of $E(k)$ that spans 10 digits. It is shown in the following section that the errors associated with the vortex method calculation itself are much larger than this.

3.2 Periodic Boundary Condition

The homogeneous isotropic turbulence is calculated using periodic boundary conditions in all directions, for both the spectral method and vortex method. The spectral method solves the Navier-Stokes equation in Fourier space (21), and considers the periodic boundary conditions exactly. On the other hand, the periodic FMM shown in section 2.2, is an approximation, where the accuracy can be controlled by adjusting the number of periodic image boxes N_{box} and the order of multipole expansion p. We must first validate the periodic FMM and show that the errors are indeed permissible.

We will first examine how the accuracy of the periodic boundary approxima-

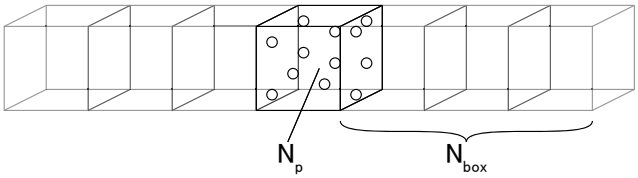

Fig. 4. Schematic of the Periodic Image Boxes

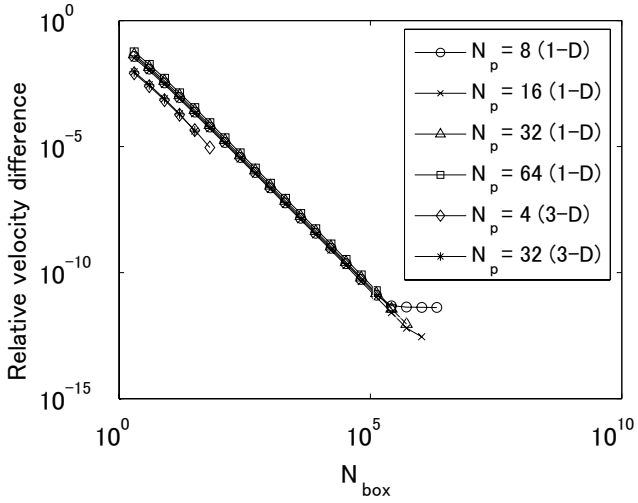

Fig. 5. Periodic Approximation Error

tion is affected by the number of particles and the number of periodic image boxes (without the FMM). This is done by placing N_p particles with random coordinates and random vortex strength within a $[-\pi, \pi]^3$ domain and copying them to the periodic image boxes, as shown in Fig. 4. The calculation is for velocity. The calculation with maximum N_{box} is used as reference to examine how the difference increases as N_{box} decreases. Results are shown in Fig. 5. The relative velocity difference is calculated by

$$\sqrt{\frac{1}{N_p}\sum_{i}^{N_p}\left(u_i - u_i^{ref}\right)^2}, \tag{23}$$

where u_i^{ref} is the velocity for maximum N_{box}. The N_{box} was increased as much as the memory permits, so the maximum value differs for different N_p. Also, N_p is extremely small compared to the actual isotropic turbulence calculation, though the difference in N_p seems to have little effect on the results.

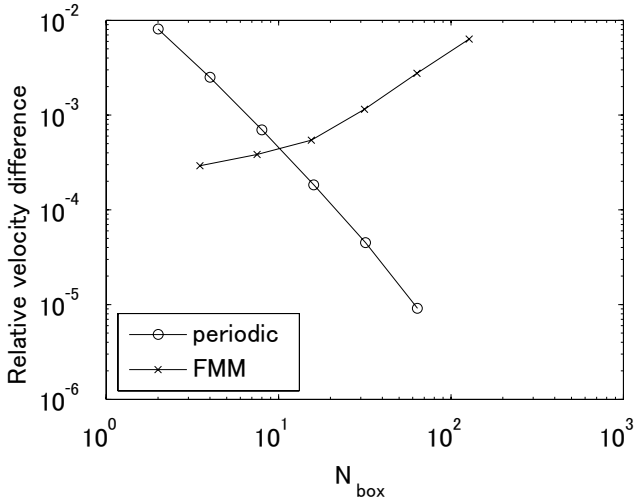

Fig. 6. Periodic FMM Error

Furthermore, the fact that distant periodic images have less impact on the total velocity does not change, even if the image boxes are distributed on a single dimension as shown in Fig. 4. Note that the calculation itself is completely 3-D, but the periodic images are distributed in only one dimension. We tested for this 1-D case first, then extended to a 3-D case, where the periodic images surround the original domain completely in all 3 dimensions. The total number of boxes is $2N_{box} + 1$ for the 1-D case, as to where the 3-D case has $(2N_{box} + 1)^3$ boxes. Due to memory limitations, the maximum N_{box} becomes quite small for the 3-D case, even for calculations with such small N_p. Nevertheless, the relative velocity difference decays at a rate proportional to N_{box}^2 for all cases, and for some cases the round-off error becomes visible. The velocity difference for the 3-D case is slightly smaller than that of the 1-D.

The FMM requires the shifting of multipole moments to larger boxes, in order to consider a larger portion of periodic images. However, shifting multipole moments to larger boxes accumulates the translation error. These FMM calculations are compared with the direct calculation using the same number of image boxes in order to assess the FMM error. The results are plotted in Fig.

6 along with the replot of $N_p = 4$(3-D) in Fig. 4. Note that the FMM calculation uses the direct calculation with the corresponding N_{box} as the reference, which have an error of their own as shown in Fig. 6 with circles. For instance, when N_{box} is small, the difference between the direct calculation and FMM is small, though the direct calculation for small N_{box} is not a credible reference. Contrary, when N_{box} is large the direct calculation is quite accurate, but the FMM starts to diverge from the direct calculation, due to the error caused by the excessive shifting of multipole moments. The actual error of the periodic FMM is the sum of the two errors shown in Fig. 6. Thus, calculating the periodic FMM up to $N_{box} = 15.5$ seems like the best choice.

3.3 Energy Spectra and Statistics

The transfer and dissipation of kinetic energy determines the shape of the energy spectrum. Therefore, if the vortex method is unable to calculate either of these correctly, it would immediately result in a discrepancy in the energy spectrum. We will first present the results of a calculation having an initial Re_λ of 25 and number of elements $N = 64^3$. The time increment is $\Delta t = 0.005$ for all calculations including the spectral method. This corresponds to a quarter of the Kolmogorov time scale, and the Courant number $u\Delta t/\Delta x$ never exceeds 0.5. No spatial refinement is performed for these calculations. The effect of spatial refinement will be considered for the PSE and CSM separately in sections 3.6 and 3.7, respectively.

The kinetic energy, enstrophy and velocity derivative moments are calculated from

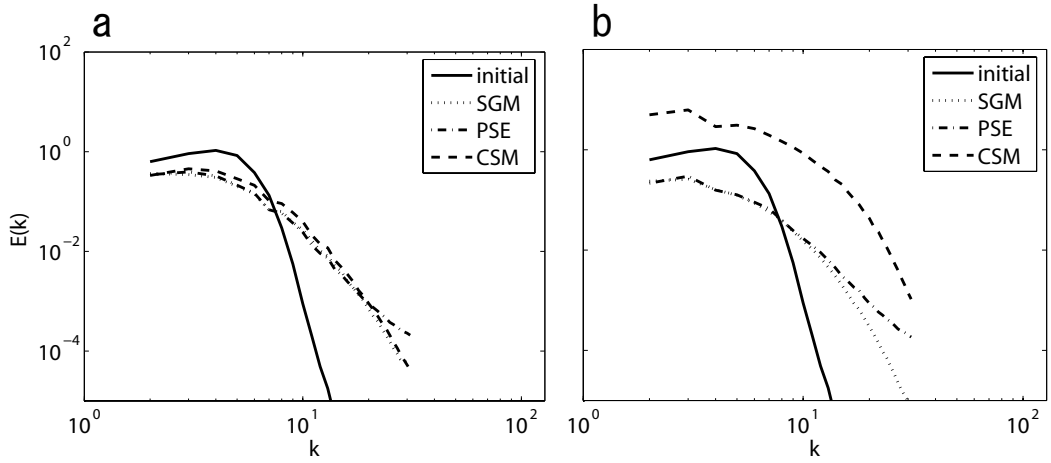

Fig. 7. Kinetic Energy Spectra for $Re_\lambda = 25$, $N = 64^3$. (a) Spectra at $t/T = 2$. (b) Spectra at $t/T = 4$.

$$K = \frac{1}{2} u_i^2, \tag{24}$$

$$\zeta = \omega_i^2, \tag{25}$$

$$F_n = \frac{\overline{(\partial u_1/\partial x_1)^n}}{\overline{(\partial u_1/\partial x_1)^2}^{\frac{1}{2}n}}. \tag{26}$$

Also, the integral scale, Taylor's micro scale, micro scale Reynolds number, and eddy turnover time have the following relation.

$$L = \frac{\pi}{2u'^2} \int k^{-1} E(k) dk \tag{27}$$

$$\lambda = \sqrt{15\nu u'^2/\epsilon} \tag{28}$$

$$Re_\lambda = u'\lambda/\nu \tag{29}$$

$$T = L/u'. \tag{30}$$

where $u' = \frac{2}{3}K$. The kinetic energy spectra for different times are shown in Fig. 7. The time t/T is in eddy turnover units, where $T = 0.25$. 'SGM', 'PSE', and 'CSM' stand for the spectral Galerkin method, particle strength exchange, and core spreading method, respectively. Note that the scaling of the vertical axis is different from Fig. 3, indicating that the initialization error is negligible for these calculations.

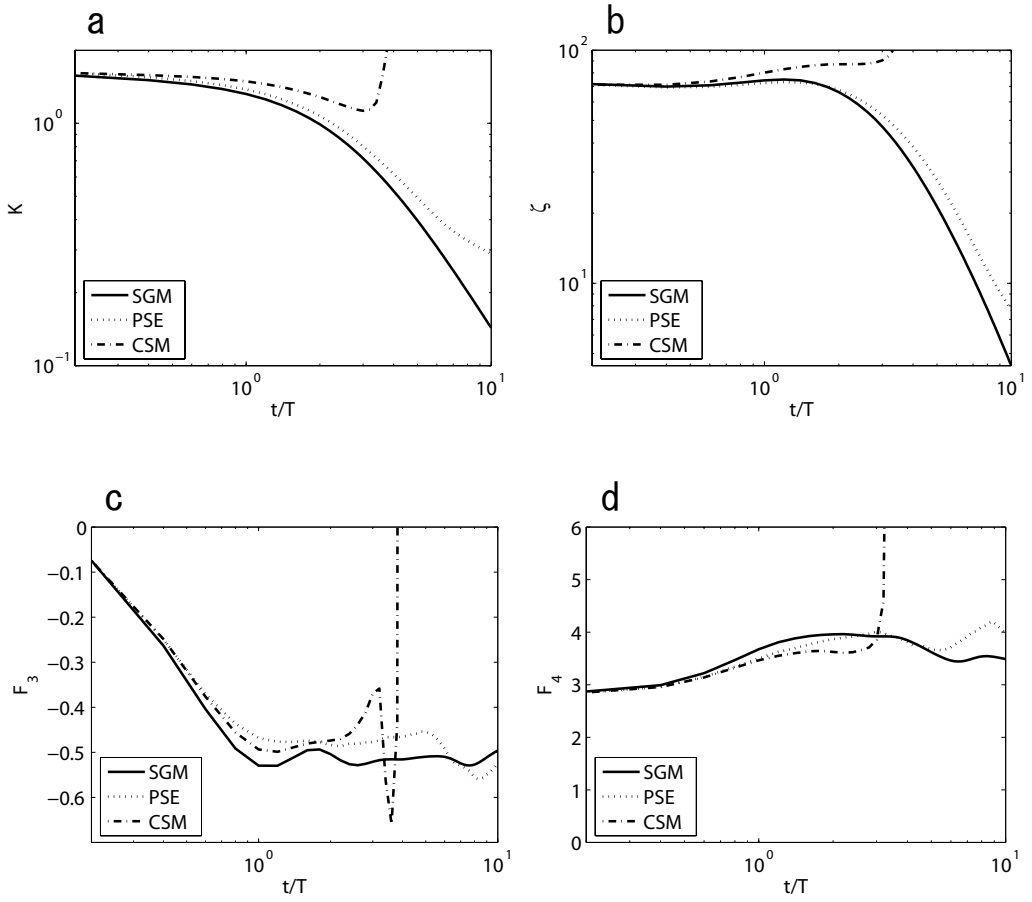

Fig. 8. Statistical Properties for $Re_\lambda = 25$, $N = 64^3$. (a) Kinetic energy. (b) Enstrophy. (c) Skewness. (d) Flatness.

All energy spectra start out from the prescribed initial spectrum, and rapidly cascade the energy down to the higher wave numbers at the earlier stages of the calculation. Once the higher wave numbers contain a certain amount of energy, the entire spectrum gradually decays. At $t/T = 2$ the three methods behave quite similarly. However, at $t/T = 4$ the CSM spectrum is about two orders of magnitude larger than the other two. Also, the PSE shows a jump at the tail of the spectrum. For these calculations the Kolmogorov scale is $\eta \approx 0.05$ and the wave number corresponding to this scale is $k \approx 20$. It can be seen that the PSE is very close to matching the SGM up to this wave number.

The energy spectrum alone is insufficient for the justification of our methods. The errors accumulating in the vortex method calculation become clear in the following time evolution plots. In Fig. 8 the time evolution of kinetic energy, enstrophy, velocity derivative skewness and flatness are shown. Their initial values are the same, but gradually diverge. The kinetic energy and enstrophy are known to show self-similar behavior at the final period of isotropic decay. This should result in a linear gradient at the end of these log-log plots. For the kinetic energy, only the SGM shows such behavior. The PSE fails to decay the kinetic energy properly at later time steps. The CSM decays only slightly, until the calculation starts to diverge at $t/T \approx 3$. For the enstrophy, the PSE shows self-similar behavior, whereas the CSM does not even decrease. The skewness and flatness of the velocity derivative behave similarly for the PSE and SGM. The CSM is able to reproduce the initial drop in the skewness but behaves strangely just prior to the blow up. Judging from the results of forced simulations for similar Re_λ by Jimenez et al. [22] and also Pumir [23] the skewness and flatness should reach the values somewhere in between $0.45 - 0.49$ and $3.5 - 4.0$, respectively. In this sense, the PSE estimates the velocity derivative moments quite well, while the flatness of the CSM prior to the blow up seems to be considerably small compared to the above mentioned criteria.

3.4 Spatial Resolution and Reynolds Number Dependence

So far, our knowledge of the performance of vortex methods is limited to a certain Reynolds number, and certain spatial resolution. One would naturally think that increasing the spatial resolution while retaining the Reynolds

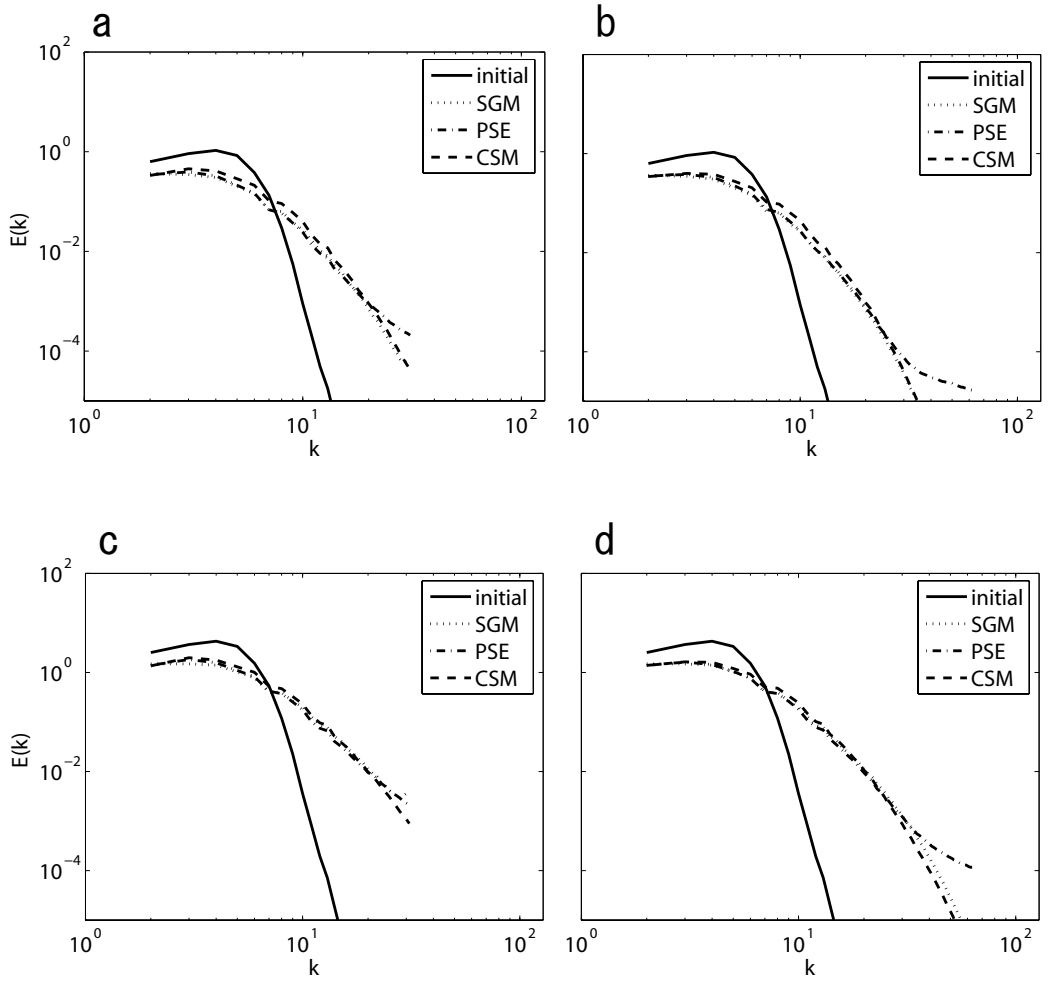

Fig. 9. Kinetic Energy Spectra at $t/T = 2$. (a) $Re_\lambda = 25$, $N = 64$. (b) $Re_\lambda = 25$, $N = 128$. (c) $Re_\lambda = 50$, $N = 64$. (d) $Re_\lambda = 50$, $N = 128$.

number would reduce the discretization errors in the calculation. Adversely, there should exist a maximum Reynolds number for which the vortex method can accurately calculate for a given number of elements. These two issues are inextricably linked, and should be investigated simultaneously.

The Reynolds number of the flow is doubled by quadrupling the strength of the prescribed energy spectrum in (22). Hence, the initial velocity fluctuation is doubled and the viscosity is unchanged. Also, the time increment is halved to account for the increase in the velocity magnitude in high Re_λ cases.

The kinetic energy spectra for 4 different cases are shown in Fig. 9. We have mentioned earlier that the Kolmogorov wave length is $k \approx 20$ for $Re_\lambda = 25$. For $Re_\lambda = 50$ it is $k \approx 30$. The spectrum of the PSE diverges from the SGM at a wave number higher than the Kolmogorov wave number for all calculation conditions except $Re_\lambda = 50$, $N = 64$. Furthermore, increasing the spatial resolution shifts the bifurcation point of the PSE to a higher wave number. On the other hand, it is difficult to tell from these plots whether or not the CSM results are improved for higher spatial resolution calculations.

The decay of kinetic energy for the 4 different cases are shown in Fig. 10. The CSM calculation diverges at $t/T \approx 3$ for all 4 conditions. For the most poorly resolved case (c), the PSE also diverges at around the same time. At this Re_λ and N even the SGM should be slightly under-resolved but it does not diverge. These results indicate that the vortex methods require more computation elements compared to spectral methods, in order to calculate high Reynolds number flows stably. It is also clear that the results of the PSE do not improve when the spatial resolution is increased.

By looking at the four cases of $Re_\lambda = 25, 50$ and $N = 64^3, 128^3$ in a comprehensive manner, the following observations can be made. Firstly, the CSM is indeed valid for a short time $t/T = 2$ and predicts the energy spectrum, kinetic energy and enstrophy decay, and also the initial drop of the velocity derivative skewness reasonably well during this finite time length. The length of this time is independent of Re_λ and N, since all calculations diverge at $t/T = 3$. Therefore, it is suspected that the divergence occurs when the overlap ratio $\sigma/\Delta x$ exceeds a certain limit, since its value is kept equal for all calculation conditions. Hence, the overlap ratio is bounded by a minimum and maximum value, and requires further investigation to ascertain the presence of an opti-

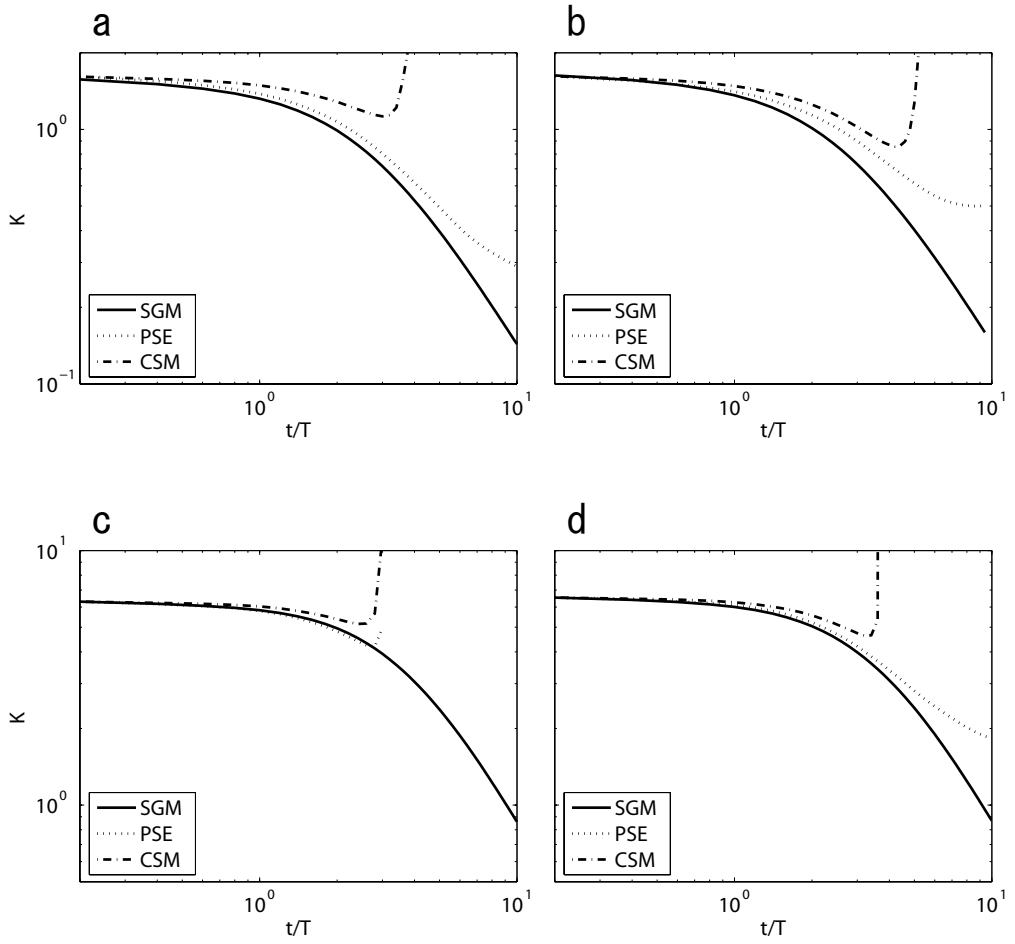

Fig. 10. Kinetic Energy Decay. (a) $Re_\lambda = 25$, $N = 64$. (b) $Re_\lambda = 25$, $N = 128$. (c) $Re_\lambda = 50$, $N = 64$. (d) $Re_\lambda = 50$, $N = 128$.

mum range. This optimum range can then be used to obtain the frequency of spatial adaption in CSMs. This issue will be considered further in section 3.7 along with the effect of spatial adaption.

Another comprehensive observation is that the PSE agrees well with the SGM for large time steps and for most configurations except the most poorly resolved case ($Re_\lambda = 50$, $N = 64^3$). Furthermore, the PSE yields higher accuracy when the spatial resolution is increased, and for these cases it matches the energy spectrum of the SGM up to the Kolmogorov wave number for a significantly long time. This fact alone, demonstrates the high accuracy of

the PSE vortex method. Though, a few problems remain unsolved. We have shown that the insufficient decay rate of the kinetic energy in PSE calculations persists for all calculation conditions. Based on the observations of the 2-D isotropic turbulence calculation [2], where the decay rate of the kinetic energy matched that of the 2-D spectral method, we suspect the problem is for the vorticity stretching term calculation, which is unique to a 3-D calculation. In the next section we will evaluate the spectral energy transfer, in order to look at the stretching term error from a different perspective.

3.5 Spectral Energy Transfer

Our main concern is how accurately the vortex method can predict the energy cascade. Plotting the energy spectra is one way to observe this. A more straightforward procedure to evaluate the spectral energy transfer would be to plot each term in the energy spectrum equation. In an isotropic turbulence the pressure terms drop out to yield,

$$\frac{\partial E}{\partial t}(k,t) = T(k,t) - 2\nu k^2 E(k,t). \tag{31}$$

The first term on the right hand side is the transfer term, which expresses the amount of energy being transferred between the wave numbers. The second term is the dissipation term, which accounts for the energy being dissipated at that particular wave number. The balance of these two determine the rate of change in kinetic energy contained in each wave number.

The terms of the energy spectrum equation for $Re_\lambda = 25$, $N = 64^3$ at $t/T = 2$ are plotted in Fig. 11. It is impossible to plot for later times because the CSM diverges shortly after this time. Plots (a)-(c) show the balance of the 3

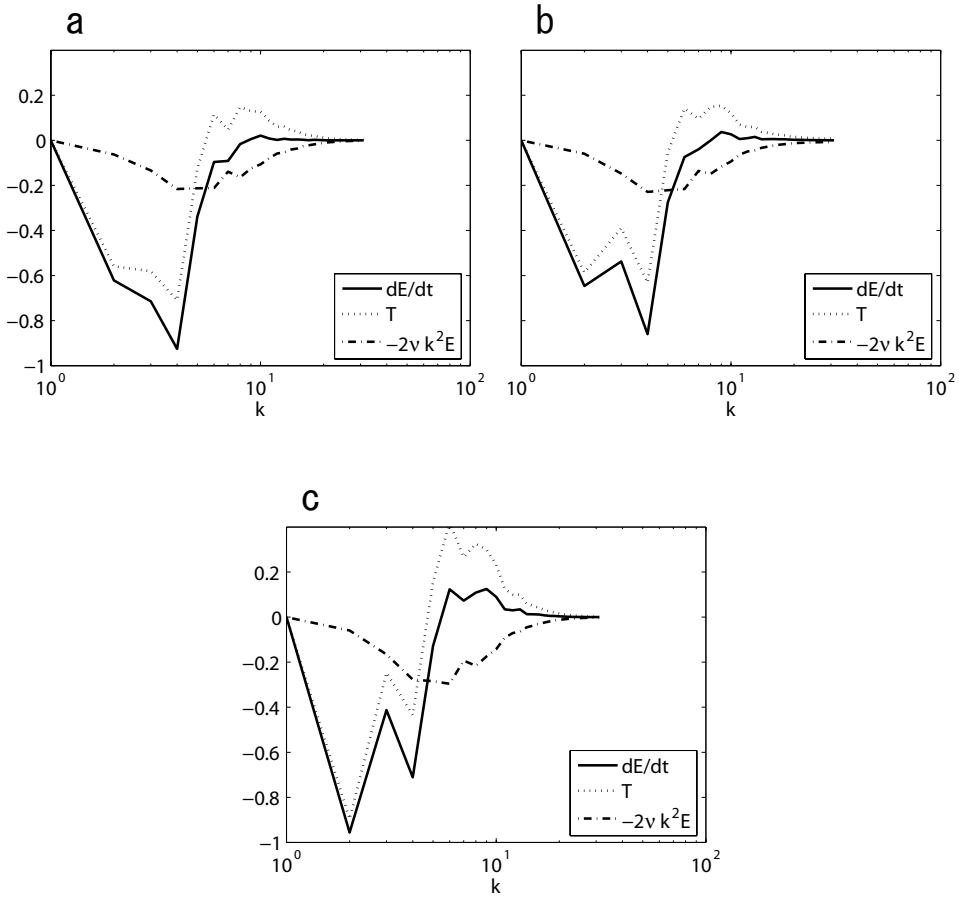

Fig. 11. Energy Spectrum Equation Budget. (a) SGM. (b) PSE. (c) CSM.

terms for each method. Although, there are some quantitative discrepancies between the 3 plots, the qualitative behavior is quite similar. The transfer term T is negative at lower wave numbers and positive at higher wave numbers, indicating that the energy is being cascaded to smaller scales. At the higher wave numbers the dissipation term has a negative peak and indicates that the kinetic energy is dissipated at smaller scales. We cannot neglect the fact that Fig. 11 (c) shows a large quantitative discrepancy between the CSM and the other two methods. Investigating the terms of energy spectrum equation has reveled further problems in the CSM, but does not clarify the insufficient decay rate of the PSE.

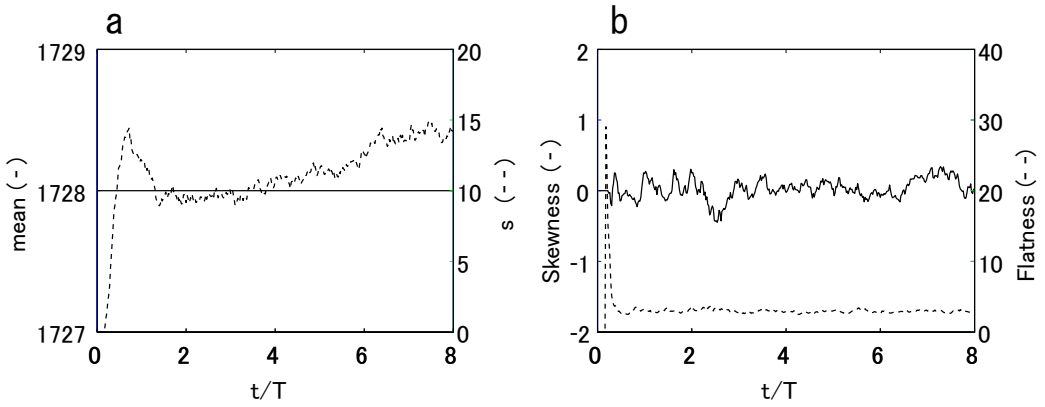

Fig. 12. Statistics of the Particle Distribution. (a) Mean & RMS. (b) Skewness & Flatness.

3.6 Spatial Adaption in PSE

As the vortex method calculation proceeds, the vortex elements become more and more disordered. This has a detrimental effect not only on the PSE diffusion calculation, but also the velocity and stretching calculations. We will first examine the particle density distribution throughout the flow field by making use of the FMM box structure. The FMM can identify and index all particles in the vicinity of any given particle. Since this box structure is what we use for the velocity, stretching and PSE diffusion calculations, monitoring the particle density using this method shows us the direct relation between the magnitude of Lagrangian distortion and the error caused by it.

We will consider the case for $Re_\lambda = 25$ and $N = 64^3$, for which the FMM divides the domain into 8^4 boxes. One box contains an average of 64 particles, so if we consider particles in the 26 neighboring boxes the total should be $27 \times 64 = 1728$. This value differs between dense regions and sparse regions, and our concern is exactly how large this difference is, and how this changes as the calculation proceeds. Fig. 12 shows the mean, standard deviation, skewness,

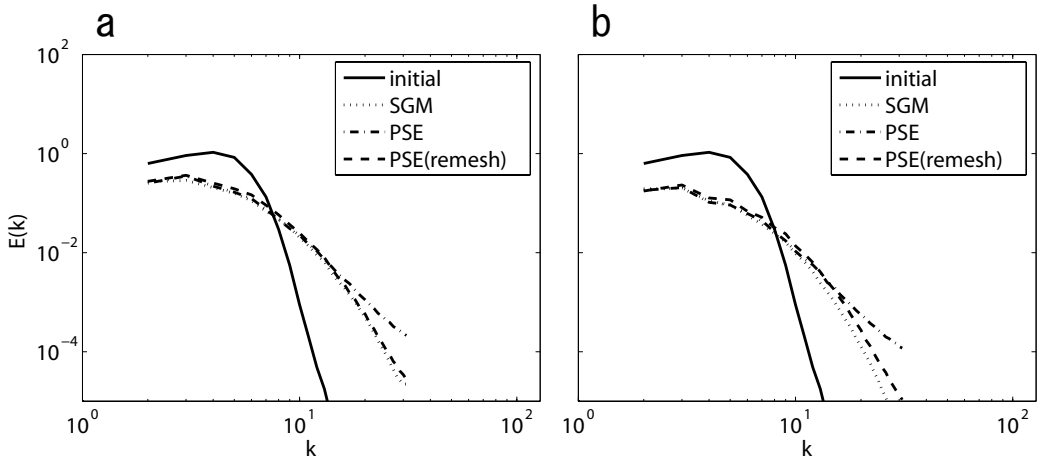

Fig. 13. Kinetic Energy Spectra for PSE with remeshing. (a) Spectra at $t/T = 2$. (b) Spectra at $t/T = 4$.

and flatness of the particle density distribution. The mean value is always 1728, since the total number of particles does not change. The standard deviation is 0 for the initially uniform distribution, and grows rapidly at the earlier stages of the calculation. Though, the increment becomes moderate at later stages and the final value is still less than 1% of the mean. The skewness fluctuates between -0.5 and 0.5, and the flatness jumps at the first few time steps but remains close to 3 otherwise, which is common for an initially uniform distribution subject to random movement.

Next, we will use a standard remeshing technique to maintain the uniformity of particles. The M_4' function is used as the interpolation formula.

$$M_4'(x) = \begin{cases} 0 & if \quad |x| > 2 \\ \frac{1}{2}(2-|x|)^2(1-|x|) & if \quad 1 \le |x| \le 2 \\ 1 - \frac{5x^2}{2} + \frac{3|x|^3}{2} & if \quad |x| \le 1 \end{cases} \tag{32}$$

The remeshing is performed every 10 times steps, which corresponds to

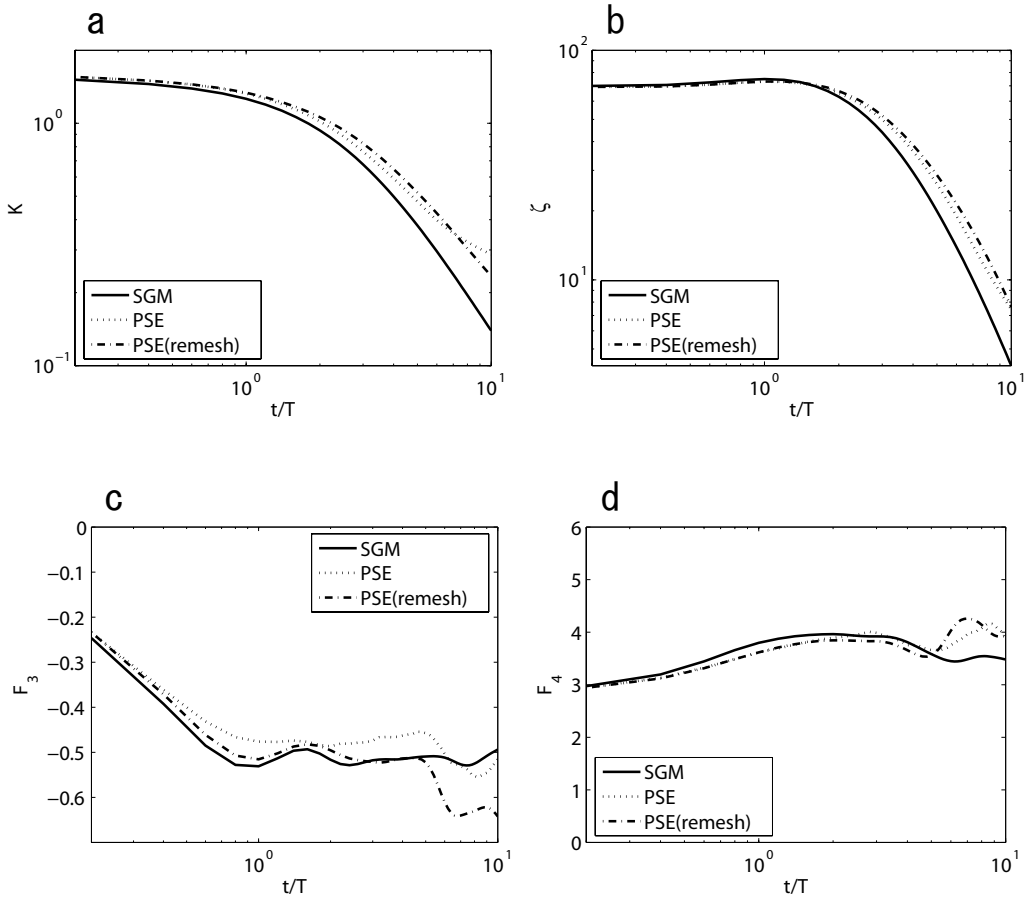

Fig. 14. Statistical Properties for PSE with remeshing. (a) Kinetic energy. (b) Enstrophy. (c) Skewness. (d) Flatness.

t/T=0.2. Judging from Fig. 12, the standard deviation of the particle density distribution should remain less than 0.1% of the mean. The kinetic energy spectra for the remeshed PSE at $Re_\lambda = 25$ and $N = 64^3$ are shown in Fig.13. The PSE without remeshing and SGM are also plotted as reference. The remeshed PSE no longer shows the jump at the tail of the spectrum. At $t/T = 2$ it matches the SGM up to the highest wave numbers. At $t/T = 4$ the remeshed PSE slightly over-predicts a broad band of the spectrum, but is much closer to the SGM than the PSE without remeshing.

The time change of statistical values for the remeshed PSE are plotted in

Fig. 14. The decay of kinetic energy has improved slightly at the end but is still different from that of the SGM. This supports our assumption that this error is caused by the error in stretching calculations, and has nothing to do with Lagrangian distortion of particles. Furthermore, when the remeshing is performed the velocity derivative skewness shows strange behavior at the end. After all, the homogeneous isotropic turbulence is a flow field with minimum Lagrangian distortion effects. For this particular flow, the only effect of remeshing seems to be the suppression of the noise at the tail of the energy spectrum, and a small improvement in the kinetic energy decay.

3.7 Spatial Adaption in CSM

The CSM is able to calculate accurately for a limited time, and diverges after that. This behavior is not only well known, but is also mathematically predictable [24]. The core radius eventually becomes too large for a sufficient spatial resolution of the local fluid motion. However, the CSM is known to converge if spatial refinement is performed either globally [8] or locally [9]. In our case, we could not use splitting methods since the calculation cost would become overwhelming for an already spatially well resolved simulation.

One way to perform spatial refinement without increasing the number of elements would be to use the radial basis function interpolation [8] for smaller sized blobs to reproduce the vorticity field. We have applied this method by solving a system of equations given by (3) for the initial core radius $\sigma = 2\Delta x$. The BICGSTAB method without preconditioning is used for the iteration, and calculated until the L^2 norm error was less than 10^{-4}. The FMM box structure was also used to calculate (3) efficiently inside the BICGSTAB iteration. At

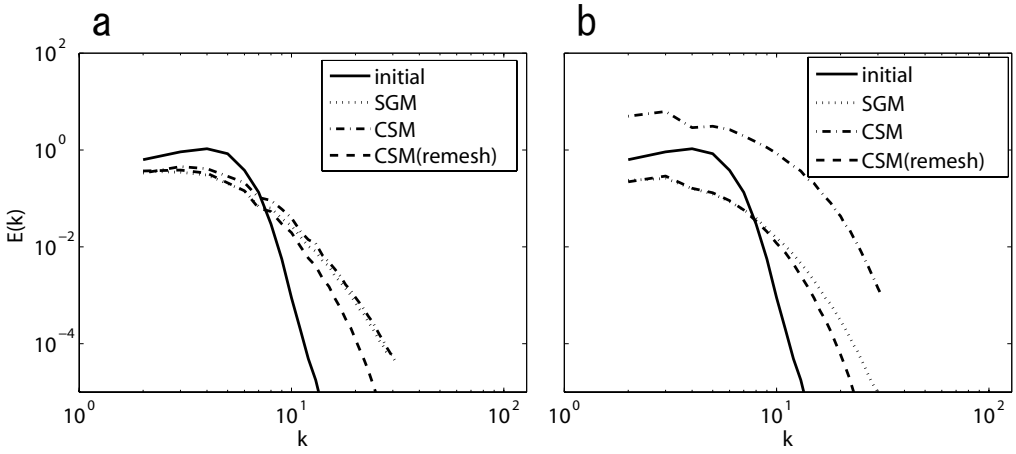

Fig. 15. Kinetic Energy Spectra for CSM with spatial adaption. (a) Spectra at $t/T = 2$. (b) Spectra at $t/T = 4$.

this point we have not found a way to significantly accelerate this procedure any further, and one spatial adaption step takes the same amount of time as 5 vortex method time steps. Hence, if we perform the spatial adaption every 5 time steps, it will double the total calculation time.

The kinetic energy spectra with spatial adaption are shown for $Re_\lambda = 25$ and $N = 64^3$ are shown in Fig. 15, along with the CSM without spatial adaption and SGM. The spatial adaption is performed every 10 time steps. 'CSM(remesh)' denotes the CSM with spatial adaption. At $t/T = 2$ the CSM with spatial adaption under-estimates the higher wave numbers. However, as the calculation proceeds, the spectrum of the CSM with spatial adaption becomes closer to the SGM. This is completely different from the CSM without spatial adaption, which diverges at $t/T \approx 4$.

Next, the kinetic energy, enstrophy, velocity derivative skewness, and flatness are shown in Fig. 16 for the same calculations. The CSM with spatial adaption almost completely matches the SGM. These results are quite encouraging, and it is fair to say that the core spreading method with spatial adaption is indeed

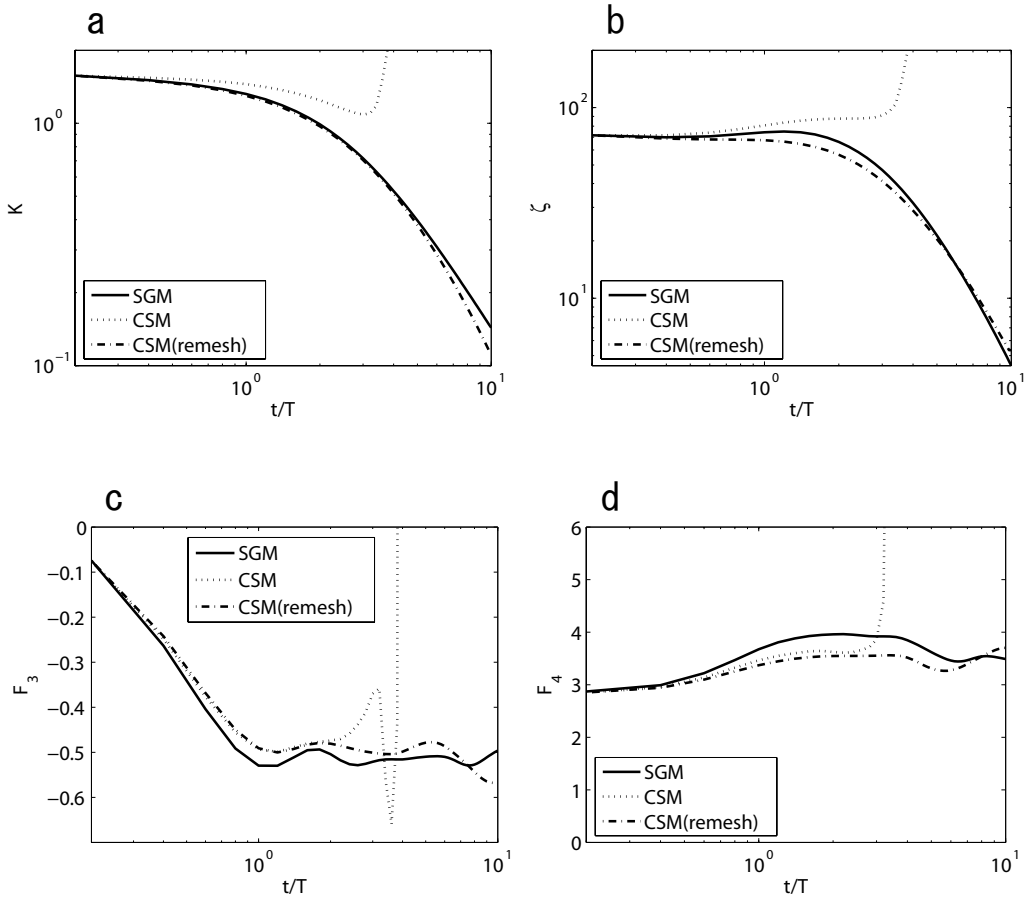

Fig. 16. Statistical Properties for CSM with spatial adaption. (a) Kinetic energy. (b) Enstrophy. (c) Skewness. (d) Flatness.

a very accurate viscous diffusion scheme.

Finally, the growth of the core radius is shown for the cases with and without spatial adaption in Fig. 17. The initial core radius is $2\pi/64 \approx 0.1$ and nearly doubles by the time $t/T = 10$ without spatial adaption. However, with the spatial adaption, the core radius increases merely 1%. We will not conduct a thorough investigation of the frequency of spatial adaption or the optimum overlap ratio range. Though, we will note that such an investigation is important and maybe inevitable in the future of pure Lagrangian vortex methods.

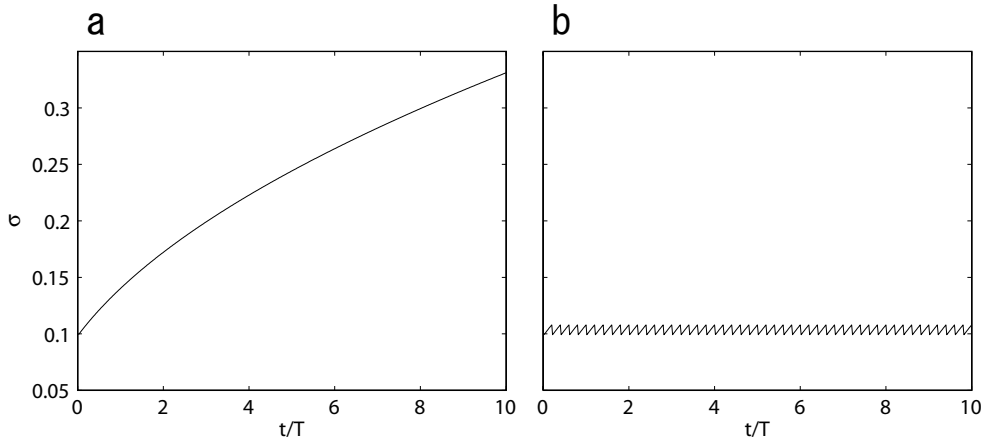

Fig. 17. Growth of the Core Radius. (a) Without Spatial Adaption. (b) With Spatial Adaption.

4 Conclusions

The vortex method is applied to the calculation of a decaying homogeneous isotropic turbulence of $Re_\lambda = 25, 50$ and the results are compared with a spectral method calculation. The core spreading method and particle strength exchange were selected as the viscous diffusion scheme, and the effect of spatial adaption was examined. The following conclusions are drawn from the results of our calculations.

For the particle strength exchange, the kinetic energy spectrum agrees well with the spectral method up to the dissipation wave number. The number of elements required however, seems to be much larger than that of the spectral method. Also, the use of remeshing has minimal effect in an isotropic turbulence, where the vortex elements remain evenly distributed.

The results of the core spreading method are only valid until $t/T \approx 2$ without spatial adaption. However, the use of the radial basis function interpolation for spatial adaption proved to be very effective. It not only keeps the calculation

from diverging, but allows the core spreading method to calculate the kinetic energy decay at an accuracy close to the spectral methods.

The overall conclusion corresponding to our initial objective is that the vortex method can reproduce the energy cascade of an isotropic turbulence correctly if the following conditions are satisfied. The spatial resolution must be satisfactory. If the PSE is used no spatial adaption is required for this flow. However, if the core spreading method is used, the spatial adaption must be performed.

References

[1] G. H. Cottet, B. Michaux, S. Ossia, G. VanderLinden, A Comparison of Spectral and Vortex Methods in Three-Dimensional Incompressible Flows, J. Comp. Phys 175 (2002) 702-712.

[2] Y. Totsuka, S. Obi, The Vortex Method Applied to Simulation of Homogeneous Isotropic Turbulence, International Conference on Computational Methods, Singapore, Dec. 15-17 (2004) FP212.

[3] S. Koshizuka, H. Tamako, Y. Oka, A Particle Method for Incompressible Viscous Flow with Fluid Fragmentation, Comput. Fluid Dyn. J. 4 (1995) 29-46.

[4] A. J. Chorin, Numerical Study of Slightly Viscous Flow, J. Fluid Mech. 57 (1973), 785-796.

[5] K. Kuwahara, H. Takami, Numerical Studies of Two-Dimensional Vortex Motion by a System of Point Vortices, J. Phys. Soc. Japan, 34 (1) (1973) 247-253.

[6] A. Leonard, Vortex Methods for Flow Simulations, J. Comput. Phys. 37 (1980) 289-335.

[7] L. F. Rossi, Resurrecting Core Spreading Vortex Methods: A New Scheme that is Both Deterministic and Convergent, SIAM J. Sci. Comput. 17 (2) (1996) 370-397.

[8] L. A. Barba, A. Leonard, C. B. Allen, Advances in Viscous Vortex Methods-Meshless Spatial Adaption Based on Radial Basis Function Interpolation, Int. J. Num. Meth. Fluids 47 (5) (2005) 387-421.

[9] M.-J. Huang, Diffusion via Splitting and Remeshing via Merging in Vortex Methods, Int. J. Num. Meth. Fluids 48 (2) (2005) 521-536.

[10] P. Degond, S. Mas-Gallic, The Weighted Particle Method for Convection-Diffusion Equations. Part 1: The Case of an Isotropic Viscosity, Math. Comput. 53 (188) (1989) 485-507.

[11] P. Chatelain, A. Leonard, Face-centred cubic lattices and particle redistribution in vortex methods, J. Turb. 3 (046) (2002).

[12] S. Shankar, L. van Dommelen, A New Diffusion Procedure for Vortex Methods, J. Comput. Phys. 127 (2) (1996) 88-109.

[13] Y. Ogami Y, T. Akamatsu, Viscous Flow Simulation Using the Discrete Vortex Model-the Diffusion Velocity Method, Comput. Fluids 19 (1991) 433-441.

[14] J. R. Grant, J. S. Marshall, Diffusion Velocity for a Three-Dimensional Vorticity Field, Theor. Comput. Fluid Dyn. 19 (6) (2005) 377-390.

[15] P. D. Koumoutsakos, G. H. Cottet, Vortex Methods, Cambridge University Press (2000).

[16] G. S. Winckelmans, Vortex Methods, The Encyclopedia of Fluid Mechanics, 3, John Wiley & Sons (2004).

[17] H. Cheng, L. Greengard and V. Rokhlin, A Fast Adaptive Multipole Algorithm in Three Dimensions, J. Comp. Phys 155 (1999) 468-498.

[18] N. A. Gumerov, R. Duraiswami, Fast Multipole Methods for the Helmholtz Equation in Three Dimensions, Elsevier (2004).

[19] C. R. Anderson, An Implementation of the Fast Multipole Method without Multipoles, SIAM J. Sci. Stat. Comput. 13 (1992) 923-947.

[20] J. Makino, Yet Another Fast Multipole Method without Multipoles-Pseudo-Particle Multipole Method, J. Comput. Phys. 151 (1999) 910-920.

[21] R. S. Rogallo, Numerical experiments in homogeneous turbulence, NASA TM-81315 (1981).

[22] J. Jimenez, A. A. Wray, P. G. Saffman, R. S. Rogallo, The Structure of Intense Vorticity in Isotropic Turbulence, J. Fluid Mech. 255 (1993) 65-90.

[23] A. Pumir, A Numerical Study of Pressure Fluctuations in Three-Dimensional, Incompressible, Homogeneous, Isotropic Turbulence, Phys. Fluids 6 (6) (1994) 2071-2083.

[24] C. Greengard, The Core Spreading Method Approximates the Wrong Equation, J. Comp. Phys. 61 (2) (1985) 345-348.